Femtosecond Time-Resolved Geometry Relaxation and Ultrafast Intramolecular Energy Redistribution in Ag_2Au

Thorsten M. Bernhardt,*[a] Jan Hagen,[a] Liana D. Socaciu,[a] Roland Mitrić,[b] Andreas Heidenreich,[c] Jérôme Le Roux,[a] Denisia Popolan,[a] Mihai Vaida,[a] Ludger Wöste,[a] Vlasta Bonačić-Koutecký,*[b] and Joshua Jortner[c]

The ultrafast dynamics of the bimetallic cluster Ag_2Au is investigated by pump–probe negative ion-to-neutral-to-positive ion (NeNePo) spectroscopy. Preparation of the neutral cluster in a highly nonequilibrium state by electron detachment from the mass-selected anion, and subsequent probing of the neutral nuclear dynamics through two-photon ionization to the cationic state, leads to strongly probe-energy-dependent transient cation-abundance signals. The origin of this pronounced time and wavelength dependence of the ionization probability on the femtosecond scale is revealed by ab initio theoretical simulations of the transient spectra. Based on the analysis of underlying dynamics, two fundamental processes involving geometry relaxation from linear to triangular structure followed by ultrafast intramolecular vibrational energy redistribution (IVR) have been identified and for the first time experimentally observed in the frame of NeNePo spectroscopy under conditions close to zero electron kinetic energy.

1. Introduction

Remarkable experimental and theoretical progress in the exploration of intramolecular, cluster, and condensed-phase femtosecond dynamics established the conceptual framework for ultrafast chemical dynamics and the timescale of nuclear motion.[1,2] Central features of ultrafast adiabatic dynamics pertain to configurational changes and intramolecular (or intracluster) vibrational energy redistribution (IVR) in vertically excited or ionized electronic-vibrational states of polyatomic molecules and clusters.[2] The exploration of nuclear dynamics triggered by vertical electronic-vibrational excitation and ionization addresses the foundations of chemical reactivity involving the transition state and accommodation of vibrational energy through IVR.

Arrhenius' picture for the path of chemical reactions was fundamentally concerned with reaction activation, which was described by his famous equation. Activation enables the system to propagate toward the transition state on the reaction coordinate, as pointed out by Wigner and by Eyring. With the advent of femtosecond spectroscopy, real-time interrogation of the transition state of chemical reactions became amenable to experimental[3–5] and theoretical[6–8] study. The underlying idea involved the preparation of a transition state of a chemical reaction by a vertical optical excitation or ionization process, which resulted in a nonequilibrium nuclear configuration of a stable collision complex, and probing its temporal evolution by laser-induced fluorescence, photoelectron spectroscopy, or resonance-enhanced multiphoton ionization spectroscopy.[3–8] In this respect, some of the present authors advanced a vertical one-photon photodetachment technique to prepare a transition state of a neutral mass-selected cluster and its subsequent interrogation by (one-photon or two-photon) ionization.[4,5] Negative ion-to-neutral-to-positive ion (NeNePo) pump–probe femtosecond spectroscopy was first applied to explore the nuclear dynamics of the transition state of the Ag_3 cluster in the nonequilibrium linear structure ($^2\Sigma_g^+$ state), and was later also extended to larger metal clusters[9] and molecules.[10] In the latter example the particular ability of the NeNePo technique to probe the transition-state dynamics of *thermal* chemical reactions was emphasized.[10] In the case of Ag_3, the relaxation dynamics include sequential processes of configurational relaxation to the triangular structure ($^2B_2$ state), intracluster collisions, and IVR.[5,7,8,11–13]

The process of IVR in an isolated molecule or cluster involves vibrational energy flow from an initially excited vibrational mode, or a wave packet of such vibrational modes, to other types of nuclear motion.[14] IVR is the manifestation of quantum coherence imposed by the preparation process on the initial state. The idea of mode selectivity in unimolecular reactions is quite old, dating to Hinshelwood in 1927–1933[15] who consid-

[a] *Dr. T. M. Bernhardt, Dr. J. Hagen, L. D. Socaciu, Dr. J. Le Roux, D. Popolan, M. Vaida, Prof. L. Wöste*
Institut für Experimentalphysik, Freie Universität Berlin
Arnimallee 14, 14195 Berlin (Germany)
Fax: (+49) 30-838-55567
E-mail: tbernhar@physik.fu-berlin.de

[b] *Dr. R. Mitrić, Prof. V. Bonačić-Koutecký*
Institut für Chemie, Humboldt-Universität zu Berlin
Brook-Taylor-Straße 2, 12489 Berlin (Germany)
Fax: (+49) 30-2093-5572
E-mail: vbk@chemie.hu-berlin.de

[c] *Dr. A. Heidenreich, Prof. J. Jortner*
School of Chemistry, Tel Aviv University
Tel Aviv 69978 (Israel)

 DOI: 10.1002/cphc.200400454

ered the possibility of "particular division of energy among a limited number of vibrational degrees of freedom." However, the seminal Rice–-Ramsperger–-Kassel–-Marcus (RRKM) theory of unimolecular reactions rested on the concept of complete IVR, although this central process was not observed at that time. During the last two decades, through the advent of ultrafast laser spectroscopy in supersonic beams, the phenomena, vibrational energy domain, and timescales of IVR became amenable to experimental interrogation. Typical examples regarding the energy domain of IVR involve the observations of Amirav et al.[16] of mode-selective intersystem crossing from the S_1 state in jet-cooled large aromatic molecules (e.g., substituted anthracenes), which are eroded as a result of IVR at an excess vibrational energy above $\approx 800\ cm^{-1}$. The energy and the time-resolved picosecond dynamics of IVR in the S_1 state of jet-cooled anthracene molecules were explored by Felker and Zewail.[17]

As a three-atom molecule or cluster is the simplest system in which IVR can occur, particular attention has been devoted to these systems.[7,8,13] Herein, we report joint experimental and theoretical results on the bimetallic noble metal trimer Ag_2Au, which allow determination of the influence of a heavy atom on the timescales of processes and of lowered symmetry on the nuclear dynamics. From the experimental side it will be shown that, by NeNePo spectroscopy under conditions close to zero electron kinetic energy (ZEKE), the timescales of different processes such as geometric relaxation versus IVR can be revealed. At the same time this has been predicted by theoretical simulations, which are capable of identifying these different processes in signals at different probe energies. Furthermore, a detailed analysis of the energy redistribution provides valuable insight into the participation of the different vibrational modes in the process of ultrafast IVR.

Experimental Section

The original NeNePo experimental setup[4,18] was extended to enable the control of cluster temperature between 20 and 300 K,[19] because only through experimental knowledge of the precise temperature of the initial cluster ensemble does a detailed comparison with theoretically simulated NeNePo transients become possible. Silver–gold mixed clusters are prepared by simultaneous sputtering of four silver–gold alloy targets (composition Ag 70:Au 30; MaTeck, Jülich, Germany) with accelerated xenon ion beams of 12 keV kinetic energy. The xenon ion beams are generated by a cold reflex discharge ion source (CORDIS[20]) and directed onto the targets by an electrostatic lens system (see Figure 1). The charged clusters sputtered from the targets are steered into a first helium-filled quadrupole Q_0, which serves to collimate and thermalize the cluster ions. The ion beam is further guided into a mass-selective quadrupole filter Q_1 to select the Ag_2Au^- ions from the initial cluster distribution. Subsequently, the monodisperse cluster beam is guided by a third quadrupole Q_2 into a helium-filled ($\approx$1 Pa) octopole ion trap. The potential on the entrance lens L_1 of this ion trap is chosen just below the kinetic energy of the ion beam so that the cluster ions are able to enter the trap (see Figure 1). They traverse the trap (80 mm length) and are reflected by the repulsive negative potential on the back electrode (exit lens L_2) of the trap. However, through collisions with the helium buffer gas inside the trap, they very rapidly lose kinetic energy and are not able to pass the entrance lens again. In this way the ions can be stored inside the rf–octopole ion trap for seconds without significant ion loss. The ion trap enclosure is attached to a closed-cycle helium cryostat, which allows variable temperature adjustment between 20 and 350 K. Thermal equilibration of the clusters entering the trap is achieved within about a thousand collisions with the buffer gas, that is, in a few milliseconds under our operating conditions.[19]

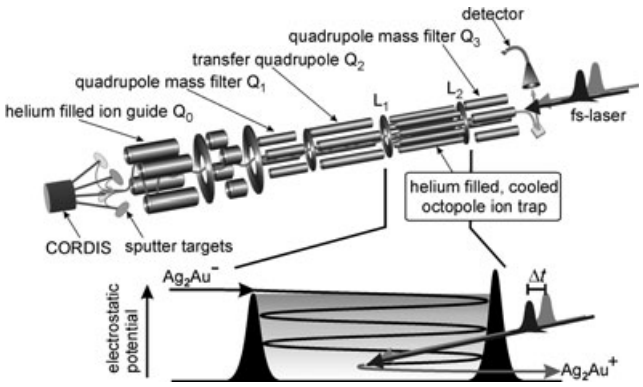

Figure 1. *Experimental setup of the temperature-controlled ultrafast NeNePo experiment. The upper part is a schematic diagram of the cluster source, quadrupole, octopole, and detector device arrangements. The lower part schematically illustrates the process of cluster cooling and trapping inside the octopole ion trap, as well as the laser-induced charge-reversal process.*

The femtosecond laser pulses are generated by a home-built Ti:sapphire oscillator (Kapteyn–Murnane-type[21]) which is continuously pumped by a 5 W Spectra Physics Millennia Nd:YVO4 laser. Pulse amplification is achieved with a Nd:YLF-laser-pumped Quantronix Odin multipass amplifier to yield 1 mJ, 40 fs, 812 nm pulses at a 1 kHz repetition rate. This beam is split and 60% intensity is directed into a TOPAS parametric amplifier to yield tunable light between 240 and 1600 nm, whereas the remaining 40% intensity is frequency-doubled in a beta barium borate (BBO) crystal. The two beams are time-delayed with respect to each other, recombined, and directed into the vacuum chamber in a direction collinear with the mass spectrometer and the ion trap axis (see Figure 1). Cross-correlation of the pump and probe laser pulses is measured directly inside the chamber through recording of the two-photon photoemission current on a polycrystalline gold surface, which can be positioned in front of the octopole entrance lens L_1. The typical time resolution obtained from these measurements is 80 fs.

The average residence time of the cluster anions in the octopole ion trap before interaction with a laser pulse is on the order of a few hundred milliseconds. The first ultrafast laser pulse then detaches the excess electron of the anion resulting in a neutral cluster in the geometry of the anion. This leads to nuclear-relaxation dynamics, which can then be probed by femtosecond time-delayed two-photon ionization of the cluster to the cationic state. As soon as cations are prepared inside the ion trap, they are extracted by the electrostatic field of the exit lens L_2 and can be mass analyzed with the final quadrupole mass filter Q_3 (see Figure 1). The ion current recorded by the detector behind Q_3 as a function of the pump–probe delay time gives rise to a transient NeNePo signal that reflects the time-dependent ionization probability of the neutral clusters caused by changing nuclear arrangements.

2. Theory and Simulations

Our theoretical approach to multistate dynamics based on the combination of ab initio molecular dynamics (MD) and classical Wigner–Moyal representation of the vibronic density matrix, which requires calculations of an ensemble of classical trajectories, allowed us to determine the timescales and nature of different ultrashort processes as well as the conditions under which they can be experimentally observed.[7,8,22–25] In the framework of NeNePo spectroscopy the following steps are needed: preparation of an initial ensemble in the anionic ground state of the cluster, one-photon detachment by the pump pulse, propagation of the system on the neutral ground state, and detection in the cationic state by a time-delayed ionizing probe pulse. For this purpose precalculated high-quality energy surfaces for small systems can be used if available,[7,8] but ab initio MD "on the fly" offers a more general alternative since it is applicable to large systems.[7,8,22–26] We showed previously that our ab initio Wigner distribution method allows for accurate simulations of pump–probe signals, which account for temperature-dependent initial conditions and for zero electron kinetic energy (NeNePo-ZEKE), as well as considering the continuum states of the detached electron and the probed cation. The latter situation corresponds to the original NeNePo experimental conditions,[4] and was first demonstrated for the example of $Ag_3^-/Ag_3/Ag_3^+$ by comparing the experimental pump–probe signals with the simulated ones.[7,8] In this case only the geometric relaxation (after electron detachment) from linear to triangular configurations of Ag_3 and the corresponding timescale dependence on the temperature were identified. In contrast, it was revealed from the simulated NeNePo-ZEKE signals that not only the geometric relaxation but also a sudden internal vibrational redistribution from the bending to the stretching mode in the triangular Ag_3 region occurs as a result of a strong repulsion of the terminal atoms.[7,8] These findings indicate that a reduction of the excess energy of the detached electron of the cation is a necessary requirement for resolving geometric relaxation and IVR. Here, conditions for the experimental realization of this prerequisite will be shown for the case of Ag_2Au.

The conceptual framework and quantitative predictive power of our semiclassical simulations based on Wigner distributions were verified by comparing the results with those of a full quantum treatment of nuclear dynamics.[13] The main features of the NeNePo-ZEKE signal of Ag_3 obtained from both theoretical treatments are in very good agreement. The timescales of the different processes are identical. The relative intensities of the signal connected with geometric relaxation versus IVR are only slightly changed, which implies that interference effects are of minor importance. These findings altogether encouraged us to extend the Wigner distribution approach to larger systems such as noble-metal tetramers in combination with ab initio MD "on the fly". Knowledge was gained from these theoretical studies about the conditions under which structural properties of gas-phase clusters (global and local minima) and isomerization processes can be observed in the framework of the NeNePo-ZEKE type of spectroscopy.[23,24]

To explore the femtosecond dynamics and to simulate time-resolved pump–probe spectra of $Ag_2Au^-/Ag_2Au/Ag_2Au^+$ clusters, our ab initio Wigner distribution approach based on the propagation of the ensemble of classical trajectories carried out "on the fly" was employed. Since this involves ab initio MD on the electronic ground states, the gradient-corrected DFT with the atomic orbital (AO) Gaussian basis set is the method of choice. Therefore the electronic structure calculations and the MD "on the fly", which involves the analytic gradients for the calculation of forces along the given electronic state, were performed using the 19-electron relativistic core potential (19e-RECP) and corresponding AO basis sets for silver and gold atoms together with the BP86 density functionals. The choice of the combination of 19e-RECP and BP86 was mandatory to obtain the required accuracy for the electronic structure and dynamics of mixed trimers. This is a consequence of the strongly pronounced relativistic effects of the Au atom, in particular with regard to the relative energy of the 6s orbital and therefore of the s–d energy gap which influences the structural properties of the ground state of neutral Ag_2Au. This issue has been verified by comparing the results using the highly correlated coupled cluster method (CCSD). Therefore a simplified methodological approach such as 1e-RECP is, from the quantitative energetic point of view, not sufficiently accurate for Ag_2Au.[23] However, the 19e-RECP systematically overestimates the ionization energies and therefore the scaling factor of 0.927 has been used throughout the paper based on the values calculated using the 1e-RECP, which has been parameterized to reproduce the experimental values for ionization potentials (IPs) of silver and gold clusters (see refs. [22, 27]).

Finally, for the simulation of the pump–probe signals we need the densities of the anionic state as the initial ensemble, of the neutral state reached after photodetachment (by the pump step), and of the cationic state after photoionization (by the probe step), as well as the laser-induced transition probabilities between the states. All these quantities can be obtained by introducing the classical approximation to the Wigner–Moyal-transformed Liouville equation for the vibronic density matrix by restriction to the lowest order in $\hbar$.

Moreover, for weak fields only first-order transition processes are considered and for short pulses Gaussian envelopes are assumed. Consequently, an analytical expression for the time-resolved NeNePo-ZEKE signal was derived[7] which gives a total occupation of the cationic state [Eq. (1)].

$$S[t_d] \sim \int d\mathbf{q}_0 d\mathbf{p}_0 \int_0^\infty d\tau_1 \exp\left\{-\frac{(\tau_1 - t_d)^2}{\sigma_{pu}^2 + \sigma_{pr}^2}\right\} \times \exp\left\{-\frac{\sigma_{pr}^2}{\hbar^2}[E_{pr} - V_{IP}(\mathbf{q}_1(\tau_1;\mathbf{q}_0,\mathbf{p}_0))]^2\right\} \times \exp\left\{-\frac{\sigma_{pr}^2}{\hbar^2}[E_{pu} - V_{VDE}(\mathbf{q}_0)]^2\right\} P_0(\mathbf{q}_0,\mathbf{p}_0) \quad (1)$$

In Equation (1), E_{pu} (E_{pr}) and σ_{pu} (σ_{pr}) are the excitation energies and durations of the pump (probe) pulses, respectively, and t_d is the time delay between the pulses. $V_{IP}(\mathbf{q}_1(\tau_1;\mathbf{q}_0,\mathbf{p}_0))$ is the time-dependent energy gap between the cationic and the

neutral electronic states at time τ_1, with the corresponding coordinates $\mathbf{q}_1(\tau_1)$ on the neutral ground-state potential energy surface (PES) and with the initial coordinates and momenta $\mathbf{q}_0$ and $\mathbf{p}_0$ given by the anionic Wigner distribution $P_0(\mathbf{q}_0,\mathbf{p}_0)$. $V_{VDE}(\mathbf{q}_0)$ represents the vertical detachment energies of the initial anionic ensemble.

The simulations of the signals involve three steps:

1) First the initial anionic Wigner phase–space distribution $P_0(\mathbf{q}_0,\mathbf{p}_0)$ has to be generated either for single vibronic states or for thermal ensembles within the harmonic approximation. In this work we use a canonical ensemble for which the Wigner distribution of each normal mode [Eq. (2)] reads:

$$P(q,p) = \frac{\alpha}{\pi\hbar}\exp\left[-\frac{2\alpha}{\hbar\omega}(p^2+\omega q^2)\right] \qquad (2)$$

with ω denoting the normal-mode frequency and $\alpha = \tanh(\hbar\omega/2k_BT)$. Equation (2) corresponds to a quantum mechanical density distribution and can be used for low or moderate initial temperatures for which anharmonicities are negligible. For high temperatures an accounting for anharmonicities becomes mandatory, so that the phase-space distribution should be better obtained from a long classical trajectory. For the low temperatures considered here, the ensemble of initial conditions necessary for the molecular dynamics in the ground state was obtained by sampling the phase-space distribution [Eq. (2)]. The last exponential in Equation (1) corresponds to the Franck–Condon transition probability after the ensemble has been photodetached by the pump step.
2) In the second step the ensemble is propagated on the neutral ground-state PES using classical MD "on the fly", which gives rise to time-dependent ionization energies V_{IP}. The transition to the cationic ground state in the probe step is given by the second exponential of Equation (1).
3) In the third step the final calculation of the signal requires an averaging over the whole ensemble. The time resolution of the signal is determined by the pump–probe correlation function (the first exponential of Equation (1)) with the probe pulse window located around the time delay t_d between the two pulses. The resolution is given by the durations of the pump and probe pulses. As a consequence of the classical approximation, quantum coherence effects are not taken into account. However, their importance is expected to be negligible for heavy atoms such as silver and gold.

3. Results and Discussion

3.1. Electronic and Geometric Structure of Ag_2Au in Different Charged States

The $Ag_2Au^-/Ag_2Au/Ag_2Au^+$ system offers an opportunity to study the dynamics of configurational changes and IVR in a bimetallic system which contains a heavy atom. In this system a transition state in the neutral ground state is reached after photodetachment, and subsequently, geometry relaxation and IVR are probed by ionization to the cationic state, as schematically shown in Figure 2. Comparing the dynamics of the

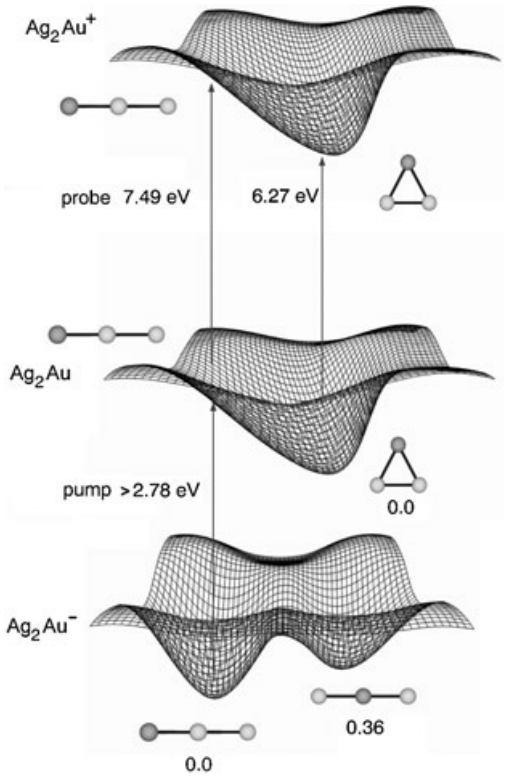

Figure 2. *Scheme for the negative ion, neutral, and positive ion of Ag_2Au. The geometries of the different isomeric structures of the anion are indicated (dark spheres: Au; light spheres: Ag). The vertical transitions from the anion equilibrium geometry to the positive ion are highlighted by arrows with the respective transition energies. Also marked by an arrow is the transition from the neutral triangular equilibrium geometry to the positive ion together with the corresponding ionization energy.*

$Ag_2Au^-/Ag_2Au/Ag_2Au^+$ system to the previously studied $Ag_3^-/Ag_3/Ag_3^+$ system, two differences are apparent: a difference in electronic structure and mass effects. In the framework of the DFT procedure with 19e-RECP and BP86 functionals, the most stable isomer in the anionic ground state assumes the linear geometry with the gold atom in a peripheral position (see Figure 2). The other linear symmetric isomer is 0.36 eV higher in energy. In the neutral ground state Ag_2Au assumes a triangular C_{2v} structure. Both linear equilibrium geometries of the anion represent transition states on the PES of the neutral. Each transition state interconnects two symmetry-equivalent triangular structures and has two imaginary frequencies along the degenerate bending mode. The NeNePo pump–probe energy scheme in Figure 2 provides information about the minimum energy required for photodetachment, and in particular about the energy interval for ionization in which minimum excess energy is transferred to the detached electron. It therefore serves as a guide for the assignment of the corresponding

pump–probe energies at which the different processes of geometry relaxation and IVR can be monitored.

3.2. Experimental NeNePo Transients at Selected Probe Energies

The experimentally determined adiabatic detachment energy of Ag_2Au^- amounts to 2.78 eV[28] (see also Figure 2). The first excited neutral state is separated from the anion by about 4 eV.[28] Pump photon energies of 446 to 310 nm should therefore be suited to preparing the neutral Ag_2Au in the electronic ground state. The transient NeNePo signals obtained do indeed show the same temporal evolution independent of the pump wavelength in this range. Figure 3a displays the NeNePo signal for 350 nm pump and 406 nm probe wavelengths measured at 20 K. An identical transient signal is obtained when the pump pulse is changed to 406 or 323 nm. The measured Ag_2Au^+ ion intensity is lowest around time zero, when the pump and probe pulses overlap temporally. The signal stays at the same low level for 1.1 ps, then rises gradually and passes a reproducible shoulder around 2.0 ps until it reaches its maximum value at 2.5 ps. It subsequently decreases again and remains almost constant at about half of its maximal intensity from 3.5 ps onward. The ionization to the cationic state is performed via a two-photon transition, which is confirmed by the quadratic power dependence of the NeNePo signal intensity.[29] Thus, the 406 nm probe pulse wavelength λ_{pr} in Figure 3a corresponds to a 6.1 eV two-photon probe energy E_{pr2ph}. Varying the probe photon energy has a dramatic influence on the temporal evolution of the NeNePo transient signal. Figure 3b shows the signal obtained with a 350 nm probe wavelength, that is, $E_{pr2ph} = 7.1$ eV. Again the Ag_2Au^+ ion intensity is minimal around time zero, but starts to rise after about 500 fs with a considerably steeper slope than that in Figure 3a to reach a maximum at 1.1 ps. The signal decreases again comparably fast and stays at a constant level after 2 ps. Finally, the NeNePo signal in Figure 3c was obtained with a probe wavelength of 323 nm ($E_{pr2ph} =$ 7.7 eV). The overall Ag_2Au^+ ion intensity is smaller compared to the two previous measurements, indicated by the smaller signal-to-noise ratio. The signal displays no peak, only a fast rise between about 700 fs and 1.5 ps to remain constant afterward within experimental accuracy.

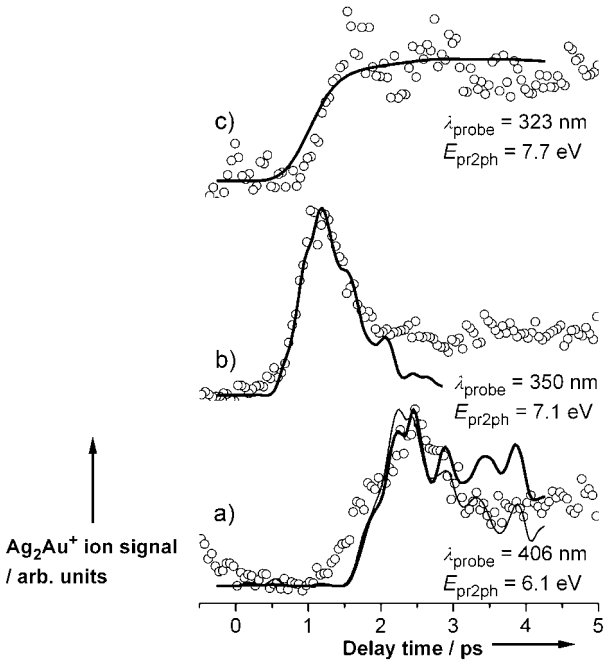

Figure 3. *Experimental NeNePo signals (○) obtained for three different probe pulse wavelengths in comparison with the simulated time-dependent signals (——) for the different probe pulse energies. The ionization probe step is two-photonic, as confirmed by power-dependent measurements. The signals are normalized in intensity: a) the experimental data obtained at $\lambda_{pr} = 406$ nm ($E_{pr2ph} = 6.1$ eV) are overlaid by the simulated NeNePo-ZEKE (bold line) and NeNePo (thin line) signals at $E_{pr} = 6.1$ eV (lower panel of Figure 7a); b) experimental data obtained at $\lambda_{pr} = 350$ nm ($E_{pr2ph} = 7.1$ eV) are overlaid by the simulated NeNePo-ZEKE signal at $E_{pr} = 7.1$ eV (second panel from the top of Figure 7a); and c) the experimental data obtained at $\lambda_{pr} = 323$ nm ($E_{pr2ph} = 7.7$ eV) are overlaid by the simulated NeNePo signal at $E_{pr} = 7.41$ eV (upper panel of Figure 7b). A common time zero between experiment and theory has been chosen for all probe energies. The deviation in the time origin corresponds to less than 0.1 eV in the probe energy.*

The theoretically obtained NeNePo signals will be presented in the following section. Their comparison to the measured time-dependent NeNePo ionization efficiencies will enable the assignment of the observed pronounced probe energy dependence to the fundamental processes of nuclear dynamics.

3.3. Selective Probing of Geometrical-Relaxation Dynamics and of IVR: Theory and Experiment

An initial temperature of 20 K, as in the experiments, was selected for the simulations. Only the most stable isomer is populated, because of the low temperature and the large energy difference between the two anionic isomers. It can also be safely assumed that the harmonic approximation is valid under these conditions. Therefore the initial conditions for the MD simulations were sampled from the canonical Wigner distribution of each independent normal mode according to Equation (2). The histogram of the vertical detachment energies (VDEs) shown in Figure 4 exhibits an almost Gaussian shape centered around 3.00 eV. The most abundant VDE is in agreement with experimental data reported in ref. [28].

In the neutral state 420 trajectories were propagated and the time-dependent energy gaps to the cationic state were calculated along the trajectories. They are required for the simulation of the NeNePo-ZEKE spectra and are shown in Figure 5. Snapshots of the neutral-state dynamics in the Cartesian center-of-mass coordinate system at selected times up to 3.5 ps are shown in Figure 6. These snapshots, together with the time-dependent energy-gap functions in Figure 5, provide information about the time evolution of the system. At $t = 0$ a localized ensemble is prepared with a very narrow spread in the coordinate space (Figure 6) corresponding to the low temperature of 20 K. After photodetachment, the system is in the transition-state region of the neutral ground-state PES and starts to evolve "downhill" (see Figure 2). The dynamics up to 1 ps are mainly characterized by a broadening of the initial en-

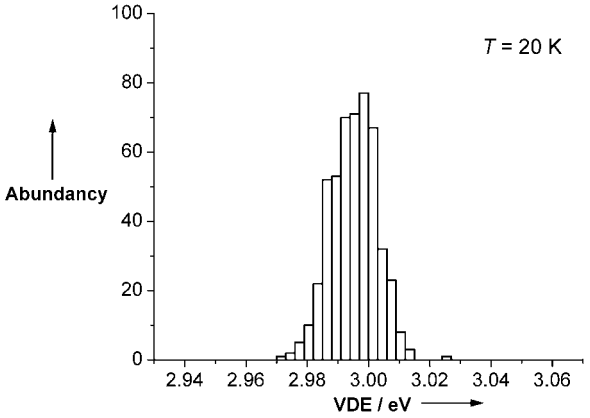

Figure 4. *Histogram of vertical detachment energies (VDEs) of Ag_2Au^- at T = 20 K.*

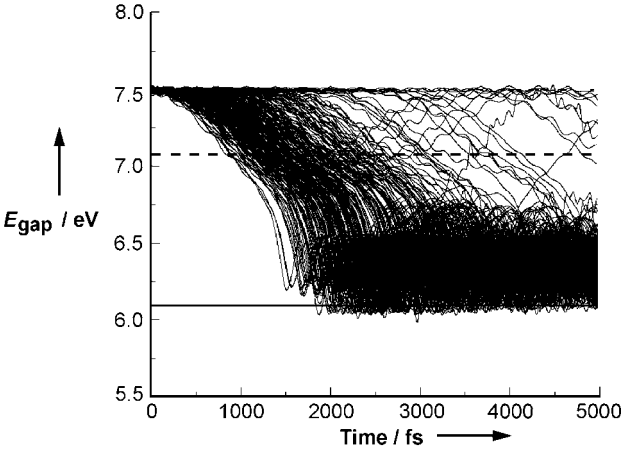

Figure 5. *Bunch of energy-gap functions (each corresponding to one simulated trajectory) between the neutral and cationic state of Ag_2Au. Ionization probe energies of 6.1 (——) and 7.1 eV (-----) are indicated. NeNePo-ZEKE spectra are obtained by integrating the contributions of the energy-gap functions that cross these lines according to Equation (1).*

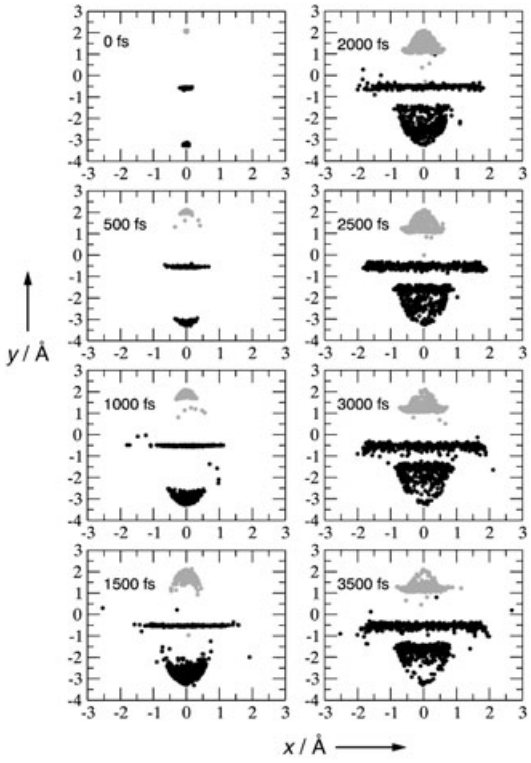

Figure 6. *Snapshots of the neutral ground-state dynamics of Ag_2Au up to 3.5 ps in the center-of-mass coordinate system in the molecular plane. Each frame shows the spatial location (x and y) of the two silver (dark dots) and one gold (light dots) atoms of an ensemble of 420 clusters at the indicated delay time. In particular, the onset of IVR is apparent from the frames at 2 ps and later times, where the distribution of the atomic locations fills a much larger area in the coordinate plane than at earlier times.*

semble, as can be seen in the first three plots of Figure 6. Consequently, the cation–neutral energy-gap functions are increasingly divergent (Figure 5). Again from Figure 6, it can be seen that the geometrical relaxation toward the triangular global minimum is complete around 1.5–2.0 ps. The onset of the geometrical change is also well-reflected by the time-dependent energy gaps in Figure 5. Within the first 2 ps, the swarm of energy gaps changes from 7.5 to 6.5 eV. Subsequently, all energy-gap functions oscillate in the interval between 6.1 and 6.5 eV, which corresponds to the vibrational dynamics within the potential-energy basin of the triangular Ag_2Au. The minimum energy-gap value of $\approx$6.1 eV marks the closest approach of the terminal silver and gold atoms, which is referred to as an internal collision within the cluster.

Regarding Figure 5, two different detection scenarios can be distinguished, both theoretically and experimentally. First is the case of a defined probe energy, denoted NeNePo-ZEKE in Section 3, a kind of resonant situation in which no energy will be transferred from the photon into the kinetic energy of the detached electron. Thus, the photon energy exactly defines the ionization energy-gap situation from Figure 5 that will show up in the positive-ion signal. These NeNePo-ZEKE signals are obtained theoretically by integrating the contributions of the energy-gap functions in Figure 5 that cross a line parallel to the abscissa which is defined by the given ionizing photon energy value. This first case is achieved experimentally by either directly detecting the zero-kinetic-energy electrons, which has not been successful so far, or by making use of a favorable resonance, either of Franck–Condon or electronic type, to approximate these conditions. The latter will be shown below to persist in the presented experimental NeNePo transients. Two essentially different kinds of processes can be probed in the NeNePo-ZEKE signals by adjusting the probe pulse energy. Pulse energies between 6.5 and 7.5 eV probe the onset of the relaxation process. It is expected that the signals in this energy range show a maximum at delay times when the probe pulse energy is resonant with the energy gaps, and decrease to zero at later times. Pulse energies below 6.5 eV serve as a probe for the arrival and the subsequent dynamics at the triangular structure. At low ($\approx$6.1 eV) pulse energies it is expected that the signal rises after 2 ps (see Figure 5) and remains almost constant at later times. The second scenario corresponds to the classical NeNePo experiment[4] in which all energy-gap values below the probe photon energy contribute

to the detected time-dependent positive-ion signal. These NeNePo transients are obtained theoretically by integrating over the contributions of all energy-gap functions in Figure 5 that propagate below a line parallel to the abscissa which is defined by the given ionizing photon energy value.

For an illustration of the different possibilities, four probe pulse energies of 7.41, 7.10, 6.84, and 6.10 eV were selected. The corresponding simulated NeNePo-ZEKE and NeNePo signals are shown in Figure 7. We first address the NeNePo-ZEKE signals (Figure 7a). The 7.41 eV pulse probes the system at the

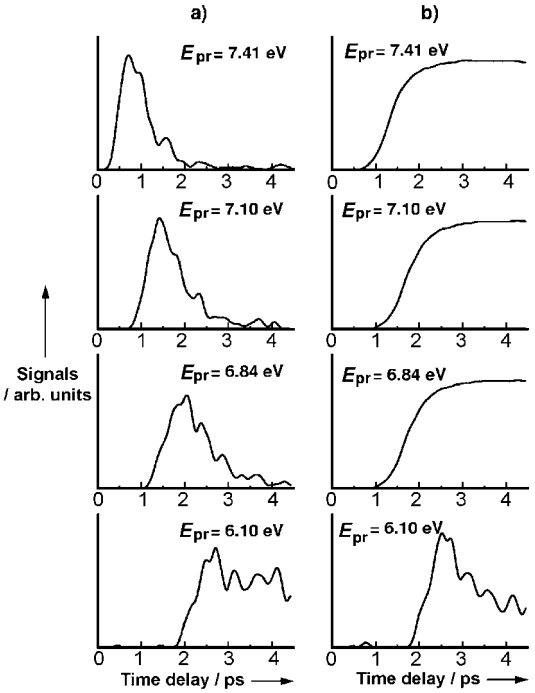

Figure 7. *Simulated NeNePo-ZEKE (a) and NeNePo (b) signals for probe energies of 6.10, 6.84, 7.10, and 7.41 eV.*

beginning of its geometrical relaxation, close to the Franck–Condon region (see Figure 2), where the Ag–Ag–Au bond angle is still large and the ionization energy high. Accordingly, the time until the onset of the signal ("incubation time") is only $\approx$200 fs and the maximum is reached at $\approx$650 fs, while at times $\geq$2 ps it drops to almost zero. The signals at 7.10 and 6.84 eV behave qualitatively similarly, but are shifted toward larger delay times (incubation times 650 fs and 1.2 ps, maxima at 1.3 and 2.0 ps, drops down toward zero at $\approx$3 and $\approx$4 ps, respectively). The signal maxima correspond to ensemble-averaged Ag–Ag–Au bond angles of 133 and 98°, respectively. The longer tail of the 6.84 eV signal reflects an increased spread of the arrival times at the probe window as a result of different initial velocities in the ensemble. However, the 6.10 eV signal rises after 2.0 ps and shows a maximum at $\approx$2.4 ps corresponding to the intracluster collision between the gold and silver atoms after arriving at the triangular structure. After passing a maximum this signal remains constant on average, and shows an irregular oscillation pattern which is characteristic for the IVR process within the triangular structure. The irregularity is a consequence of a large excess energy of 0.31 eV gained during the relaxation process. In contrast, the simulated NeNePo signals shown in Figure 7b exhibit slightly increasing incubation times on lowering the probe energy from 7.41 to 6.84 eV, followed by a monotonous increase and saturation of the signal. For the probe energy of 6.1 eV the continuum energy is so low that the simulated NeNePo-ZEKE and NeNePo signals exhibit very similar features. The comparison of both types of signals in Figure 7 clearly shows that only NeNePo-ZEKE-type experiments have a chance to resolve timescales for different processes such as geometric relaxation versus IVR.

An overlay of the experimental transients with the theoretically obtained signals at the corresponding probe energies is displayed in Figure 3. As predicted, at E_{pr2ph} = 6.1 eV (Figure 3a) the onset of IVR and the dynamics of Ag_2Au initiated by the collision of the terminal Au and Ag atoms can be probed exclusively. The good agreement between experimental and simulated NeNePo-ZEKE signals is apparent, and indicates that the experimental signal starts to rise when the system approaches the triangular potential well. The signal maximum can be assigned to the time of intracluster collision at $\approx$2.4 ps followed by IVR in the potential minimum of the neutral triangular geometry (see Figure 2). The experimental signal offset at longer delay times is somewhat lower with respect to the maximum than that expected from the simulated NeNePo-ZEKE signal. This might be attributed to contributions from the rather similar NeNePo-type signal (see Figure 7b). This shows explicitly in which regime ZEKE conditions hold in the experiment. Figure 3b shows the comparison of simulated and experimental transient-ion signals at 7.1 eV probe photon energy. The initial peak of the experimental transient is perfectly matched by the simulated NeNePo-ZEKE signal at the corresponding wavelength. Therefore the experimental conditions in this case allow for direct exclusive probing of the geometrical relaxation of Ag_2Au passing through bending angles of φ = 166° at the signal onset around 500 fs, to φ = 138° at the signal maximum, and finally up to φ = 96° at 2 ps, where the terminal atoms interact and the intracluster collision is closely ahead (see also the discussion in Section 3.4 below). The experimental signal offset at times later than 2 ps can again be attributed to the imperfect NeNePo-ZEKE conditions. Possible reasons for the good agreement of the experimental transient signal with the simulated NeNePo-ZEKE transient signal might be either a particularly favorable Franck–Condon overlap in the case of 7.1 eV two-photon probe energy or, in principle, the involvement of a hitherto unknown intermediate resonant state in the 350 nm two-photon ionization of neutral Ag_2Au. In fact, such two-photon selective NeNePo probing by resonant excited neutral states has been reported in the case of Ag_3.[12,18,19] If the transient signal of Ag_2Au at 350 nm is indeed a result of a resonant two-photon ionization process, in contrast to ionization at 406 nm, the relative intensity of the 350 nm signal should be much higher than that of the 406 nm signal. However, the signal intensities at 350 and 406 nm probing are comparable,[29] and thus resonant two-photon ioniza-

tion can be ruled out and the prevalence of a favorable Franck–Condon window is likely to be the origin of the observed signal for Ag_2Au at $E_{pr2ph}=7.1$ eV. Finally, at high ionization energy $E_{pr2ph}=7.7$ eV the theory would predict no observable time-dependent NeNePo signal, because the photon energy is high enough to ionize the neutral cluster in any geometrical arrangement. Nevertheless, a comparably weak experimental transient signal is detected. This signal is in agreement with the simulated NeNePo transient at a probe energy of 7.41 eV, just below the highest theoretically predicted ionization energy which corresponds to the linear transition-state structure (see Figure 3c). Thus, the experiment at $E_{pr2ph}=7.7$ eV apparently monitors the system when it leaves this transition-state region. Still, there is a considerable signal onset time of about 700 fs which reflects the very shallow slope of the PES around the linear transition-state geometry (see Figure 2). A possible reason for the experimental detection of a time-dependent signal at energies higher than the highest calculated ionization potential might again be found in a photon-energy-dependent Franck–Condon factor between neutral and positive-ion PES around the linear geometry, which is not considered in the simulations. However, as soon as the wavepacket has left the initial transition-state region, all structures with a smaller bending angle can be ionized and the signal in Figure 3c displays a constant offset, as does the simulated NeNePo transient.

In summary, at a 7.7 eV two-photon ionization energy Ag_2Au is monitored immediately when it leaves the linear transition-state region. Probing at $E_{pr2ph}=7.1$ eV directly detects the neutral Ag_2Au system undergoing a bending motion from an almost linear arrangement at $\varphi=166°$ to $\varphi=96°$ just before the intracluster collision. Finally, at 6.1 eV two-photon probe energy, the system is caught at the time of the collision of the terminal Ag and Au atoms at ≈ 2.4 ps which is followed by IVR in the potential minimum of the neutral triangular geometry.

3.4. Energy Accommodation: Analysis of IVR.

From our analysis of the nuclear dynamics we wish to address the timescales and the nature of the IVR. The evolution of the system can be followed from Figure 8, which shows a bundle of trajectories projected on the plane spanned by the bending coordinate (Q_b) and by the first, antisymmetric stretching (Q_{s1}) normal coordinate. The geometry relaxation involves mainly the bending and the antisymmetric stretching mode, as the motions along these coordinates are 4 and 3 Å, respectively, while the motion along the second, symmetric stretching coordinate spans only 1 Å. At the pump instant ($t=0$), the system is in the linear configuration at $Q_b=4.0$ Å, $Q_{s1}=-2.8$ Å and starts running toward the triangular equilibrium geometry at $Q_b=0$, $Q_{s1}=0$, where the trajectory bundle branches because of the appearance of IVR.

For an analysis of the vibrational energy redistribution, we decomposed the kinetic energy into normal-mode contributions. This was achieved by projecting the atomic velocities at regular time intervals on the non-mass-weighted normal coordinates of the neutral triangular Ag_2Au system. Figure 9a

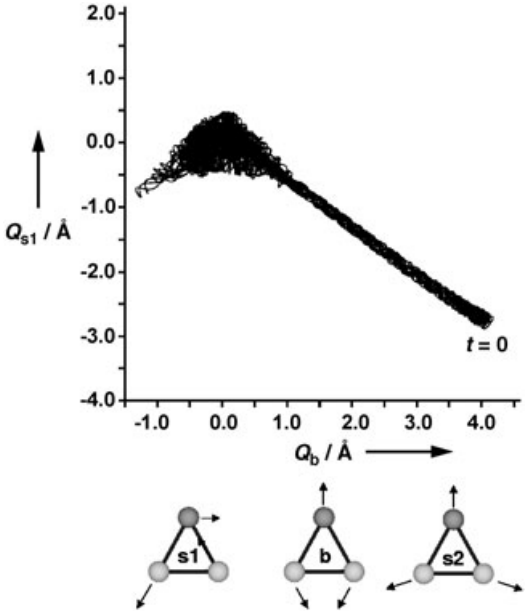

Figure 8. *Representation of a bundle of 7 trajectories in the plane spanned by the bending coordinate Q_b and by the antisymmetric stretching coordinate Q_{s1}. The starting point t = 0 is marked in the figure.*

shows a single-trajectory example together with the two distinct Ag–Ag–Au bond angles φ. The potential energy function $V(\varphi)$ for Ag_2Au is shown in Figure 10a. The bond angle φ in Figure 9a decreases from an initial value of about 180° at $t=0$ to a minimum value of 54° at $t=2.36$ ps. However, the kinetic energy begins to increase notably only at $t\geq 2.0$ ps, when φ falls short of $\approx 90°$, that is, where the steep region of $V(\varphi)$ (Figure 10a) is entered. Accordingly, within the next 360 fs φ decreases much more rapidly (Figure 9a) and the kinetic energy in the bending mode passes a pronounced maximum. Shortly after, the kinetic energy decreases to zero, as the system passes the potential minimum and the terminal atoms subsequently further approach each other ("internal collision"), until the kinetic energy is consumed by running against the repulsive part of the potential. In parallel to the increase of the kinetic energy in the bending mode, intense oscillations are triggered in the first, antisymmetric stretching mode and to a smaller extent in the symmetric stretching mode Q_{s2}. Apparently, the simultaneous gain of kinetic energy of the Q_b and Q_{s1} modes is a consequence of the fact that both normal coordinates together make up the major components of the linear-to-triangular geometric relaxation coordinate.

An analysis of the energy exchange between the modes requires the monitoring of the total energy content in each mode. The vibrational periods of the nearly periodic stretching modes (Figure 9a) can be inferred from the kinetic energy oscillations as being 306 and 204 fs, respectively. These vibrational periods reflect the corresponding harmonic values of 289 and 189 fs, prolonged by the anharmonicities. In contrast, the bending mode is completely aperiodic. Typically, the intense kinetic energy peaks of the bending mode appear in pairs, one peak with a gentle increase followed by a steep drop-off, and the second with an inverse shape. The steep side of the peak

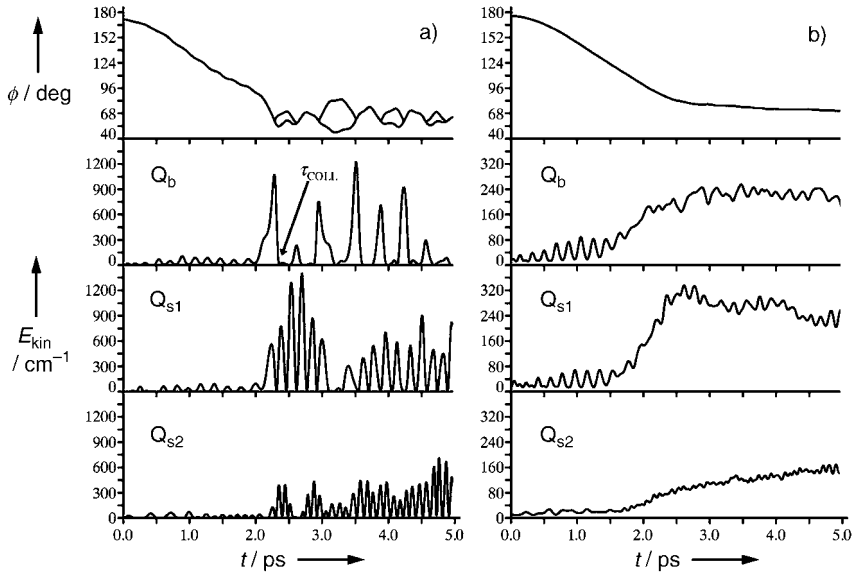

Figure 9. *a) A single-trajectory example of the evolution of the Ag–Ag–Au bond angle φ (upper panel) and of the kinetic energy in the three vibrational normal modes (lower panels). In the upper panel two functions are given for φ, since for triangular geometries two Ag–Ag–Au bond angles can be defined. The lower curve for φ reflects the atom connectivities of the initial linear geometry, and therefore monitors the geometrical relaxation until the closest approach of the terminal atoms (internal collision). The upper curve is the larger of the two Ag–Ag–Au bond angles and indicates partial escapes from the potential well of the triangular geometry. A partial escape from the potential well (see Figure 10a) with $\varphi \approx 80°$ is observed at 3.0–3.5 ps, where the oscillation of the kinetic energy of the stretching modes is very weak. In the second panel from the top, the collision time $\tau_{COLL} = 2.36$ ps, determined from the first pronounced rise and the subsequent sharp minimum of the kinetic energy in the bending mode, is marked in the diagram. b) The time evolution of the bond angle and of the kinetic energy in the vibrational normal modes, averaged over 400 trajectories.*

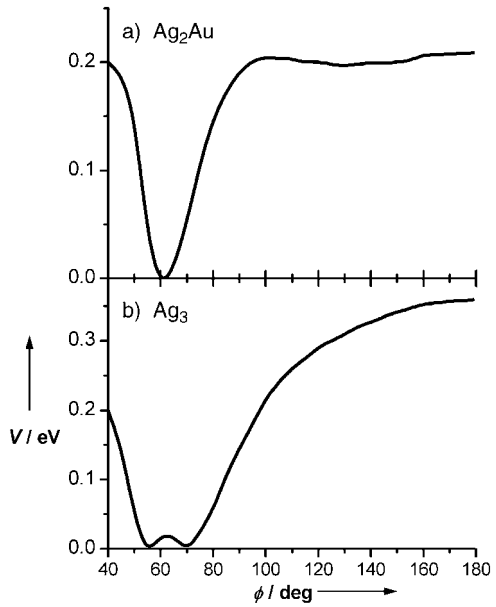

Figure 10. *The potential energy $V(\varphi)$ of Ag_2Au as a function of the bending angle (a) in comparison to the Ag_3 potential (b). Note the considerably narrower potential well around $\varphi \approx 60°$ in the case of Ag_2Au.*

marks an approach to or a departure from an internal collision, and the gentle side an increase of φ with a partial escape from the deep part of the potential well. Accordingly, intense kinetic energy oscillations of the stretching modes appear between two pronounced kinetic energy maxima of the bending mode, when the system is in the deep region of the potential well ($50° \leq \varphi \leq 80°$, see Figure 10a), so that enough energy is available for the stretching modes. This relation is particularly apparent for the antisymmetric stretching mode, and manifests an extensive energy exchange and a close coupling of these modes. In the single-trajectory example given in Figure 9a, a partial escape from the potential well with $\varphi \approx 80°$ occurs at $t = 3.0$–3.5 ps.

Insight into the IVR can be gained from an analysis of the single-trajectory example (Figure 9a). At times $t < 2.0$ ps, the three vibrational modes contain very little energy according to the envelope of their kinetic energy oscillations. This is because the system is located in the flat region of the PES, where the bond angle φ exceeds 90° (Figure 10a). In this region, the potential energy is high, but can be viewed as a constant offset, which is not available for the vibrational modes. The small envelopes of the kinetic energy oscillations are almost constant, which implies only very little IVR in this time domain. At times $t \geq 2.0$ ps the system enters the deep part of the potential well, so that the kinetic energy of all modes increases. At $t = 2.28$ ps, the kinetic energy in the bending mode reaches a sharp maximum. According to the envelopes which can be drawn around the kinetic energy maxima, the total energies of the two stretching modes can be estimated as 676 and 226 cm^{-1}, respectively, while the kinetic energy of the bending mode is 1078 cm^{-1}. The sum of the two estimated total-mode energies and of the kinetic energy of the bending mode is 1984 cm^{-1}, while the total vibrational excess energy is 1739 cm^{-1}. The deviation, 245 cm^{-1}, between these two values marks the magnitude of the error of the energy partitioning. Shortly after the bending mode has passed its maximum kinetic energy, its kinetic energy drops to zero (manifesting internal collision), which for the single trajectory of Figure 9a occurs at 2.36 ps. Since the other mode energies increase at the same time, IVR is manifested; the drop of the kinetic energy in the bending mode cannot be solely explained by a conversion of kinetic to potential energy in the bending mode. Since this behavior is also found for other trajectories, one can generally state that notable IVR sets in at the instant of internal collision.

Figure 9b shows the energy content in the three vibrational normal modes, averaged over the ensemble of 400 trajectories.

The kinetic energy in the three vibrational modes begins to rise at $t = 1.5$–2.0 ps, when the majority of the ensemble reaches the deeper part of the potential well. The larger energy content in the bending mode and in the first stretching mode reflects the initial excitation of these modes by the geometric relaxation. In a histogram of the collision times of the entire trajectory ensemble (not shown), the onset of internal collisions τ_{COLL}^{ON} is observed at 1.5 ps, which marks the onset of IVR in the system. An equipartition of the energy among the modes is not achieved within the simulation time of 5 ps. Also, the oscillations of the kinetic energy in the modes are not completely smoothed down, which indicates that the dynamics of the system is not completely dephased within 5 ps. The incomplete equipartition of energy and the incomplete dephasing suggest that 5 ps is not sufficient to equilibrate the system.

In summary, after the pump step the neutral Ag_2Au system undergoes a geometric relaxation from a linear transition state toward the triangular equilibrium configuration. The system runs downhill on the PES. At time $\tau \approx 1.5$ ps, the system starts to reach the well of the potential $V(\varphi)$ (see Figure 10a). Shortly after, the terminal atoms are so close that they repel each other. This is the time of the internal collision $\tau_{COLL}^{ON} = 1.5$ ps, which marks the end of the geometrical relaxation and the onset of IVR. The vibrational energy flows mainly from the bending to the first, antisymmetric stretching mode.

3.5. Comparison with Ag_3

The gross features of the Ag_2Au nuclear dynamics are similar to those of Ag_3, that is, a linear-to-bent geometrical relaxation with an internal collision of the terminal atoms, induction of intense oscillations, mainly of one stretching mode, and a reversible energy exchange between one stretching mode and the bending mode.[4,7,8,12,18] However, in Ag_2Au the antisymmetric stretching mode is the primary target of the initial energy transfer, whereas in Ag_3 the primary energy transfer is into the *symmetric* stretching mode.[7,8] Also, the relative kinetic energy content in the two stretching modes of Ag_2Au after our theoretical simulation time window of 5 ps is still clearly in favor of the antisymmetric stretch by 80 cm^{-1}, which underlines the fact that IVR is not completed after 5 ps in Ag_2Au. In Ag_3, the energy is equipartitioned between the antisymmetric and the symmetric stretch within 3 ps.[7,8] For Ag_2Au as well as for Ag_3, almost no IVR is observed prior to the onset τ_{COLL}^{ON} of the internal collision. The times τ_{COLL}^{ON} for Ag_3 are 990 fs for a 50 K and 750 fs for a 300 K ensemble, whereas for Ag_2Au τ_{COLL}^{ON} is 1.5 ps for an ensemble of 20 K initial temperature. Since the collision times are very much dependent on the initial ensemble temperature, the results for Ag_2Au and Ag_3 cannot be directly compared, but the timescales are in general longer in the bimetallic trimer because of the heavy Au atom. Ag_3 shows a difference after its geometrical relaxation. The probability density of Ag_3 is much less confined to the triangular equilibrium geometry than that of Ag_2Au. The reason becomes apparent when comparing the two potential functions $V(\varphi)$ depicted in Figure 10. The deep part of the potential curve spans a much narrower range for Ag_2Au (Figure 10a), while the wider Ag_3 potential (Figure 10b) favors a partial escape from the triangular configuration. In the case of Ag_2Au the bonding in the triangular structure is stronger as a result of charge transfer from Ag to Au caused by the electronegativity difference between these two atoms, which gives rise to a narrower and deeper potential well.

4. Conclusions

Temperature-controlled measurements of the neutral bimetallic cluster Ag_2Au in a femtosecond pump–probe negative ion-to-neutral-to-positive ion (NeNePo) experiment reveal the timescales of different processes of geometrical-relaxation dynamics. The experimental data are in complete agreement with first-principles ab initio molecular dynamics simulations, which provide insight into the fundamental processes of structural dynamics in this model-type triatomic system, namely geometry relaxation and IVR. Probing at a 7.1 eV two-photon ionization energy monitored directly how the neutral Ag_2Au system undergoes a bending motion from a linear transition state toward the triangular equilibrium configuration. In contrast, at a 6.1-eV two-photon probe energy, the system is caught at the time of the collision of the terminal Ag and Au atoms (intracluster collision), which marks the end of the geometrical relaxation and the onset of IVR. Detailed analysis of the energy flow in the process of IVR is provided by decomposition of the total kinetic energy of the system into normal-mode contributions. This analysis reveals that the vibrational energy flows mainly from the bending to the first, antisymmetric stretching mode and that the onset of IVR occurs on a longer timescale for the Ag_2Au cluster than for the Ag_3 cluster, because of the heavy atom.

This successful collaborative effort of first-principles calculations and femtosecond time-resolved NeNePo experiments under well-controlled conditions, such as low temperature and photoexcitation close to ZEKE conditions, demonstrates the potential of the technique to launch and assess dynamics specifically for the neutral electronic ground state. One main advantage of this approach is the fact that no electronic decay channels are provided from the neutral electronic ground state for the initial excitation and, thus, the observed dynamics can be directly attributed to vibrational-mode coupling, that is, IVR is monitored directly. Our experimental and theoretical work will be extended to structural dynamics in larger clusters, and also in particular to reactions in the neutral electronic ground state, where the analysis of the contribution of IVR is essential for a conceptual understanding of observed reaction pathways.

Acknowledgements

Technical support by Marcel Krenz is gratefully acknowledged. The authors thank the Deutsche Forschungsgemeinschaft for financial support through SFB 450: "Analysis and Control of Ultrafast Photoinduced Reactions".

Keywords: femtochemistry · gold · mass spectrometry · metal clusters · silver

[1] a) A. H. Zewail, *Femtochemistry: Ultrafast Dynamics of the Chemical Bond*, World Scientific, Singapore, **1994**; b) J. Manz, L. Wöste, *Femtosecond Chemistry*, VCH, Weinheim, **1995**; c) M. Chergui, *Femtochemistry: Ultrafast Chemical and Physical Processes in Molecular Systems*, World Scientific, Singapore, **1996**.

[2] V. Sundström, in *Nobel Symposium*, *Vol.* 101, Imperial College Press, London, **1997**.

[3] a) A. H. Zewail, *Faraday Discuss. Chem. Soc.* **1991**, *91*, 207; b) A. Mokhtari, P. Cong, J. L. Herek, A. H. Zewail, *Nature* **1990**, *348*, 225; c) M. Dantus, R. M. Bowman, M. Gruebele, A. H. Zewail, *J. Chem. Phys.* **1989**, *91*, 7437; d) A. Weaver, R. B. Metz, S. E. Bradforth, D. M. Neumark, *J. Chem. Phys.* **1990**, *93*, 5352; e) R. B. Metz, D. M. Neumark, *J. Chem. Phys.* **1992**, *97*, 962; f) D. M. Neumark, *Acc. Chem. Res.* **1993**, *26*, 33; g) S. M. Burnett, A. E. Stevens, C. S. Feigerle, W. C. Lineberger, *Chem. Phys. Lett.* **1983**, *100*, 124; h) K. M. Ervin, J. Ho, W. C. Lineberger, *J. Chem. Phys.* **1989**, *91*, 5974; i) P. G. Wenthold, D. Hrovat, W. T. Borden, W. C. Lineberger, *Science* **1996**, *272*, 1456.

[4] S. Wolf, G. Sommerer, S. Rutz, E. Schreiber, T. Leisner, L. Wöste, R. S. Berry, *Phys. Rev. Lett.* **1995**, *74*, 4177.

[5] R. S. Berry, V. Bonačić-Koutecký, J. Gaus, T. Leisner, J. Manz, B. Reischl-Lenz, H. Ruppe, S. Rutz, E. Schreiber, S. Vajda, R. de Vivie-Riedle, S. Wolf, L. Wöste, *Adv. Chem. Phys.* **1997**, *101*, 101.

[6] O. Rubner, C. Meier, V. Engel, *J. Chem. Phys.* **1997**, *107*, 1066.

[7] M. Hartmann, J. Pittner, V. Bonačić-Koutecký, A. Heidenreich, J. Jortner, *J. Chem. Phys.* **1998**, *108*, 3096.

[8] M. Hartmann, J. Pittner, V. Bonačić-Koutecký, A. Heidenreich, J. Jortner, *J. Phys. Chem. A* **1998**, *102*, 4069.

[9] a) L. Wöste, *Z. Phys. Chem. (Muenchen Ger.)* **1996**, *196*, 1; b) H. Hess, K. R. Asmis, T. Leisner, L. Wöste, *Eur. J. Phys.* **2001**, *16*, 145.

[10] D. H. Paik, D.-S. Yang, I.-R. Lee, A. H. Zewail, *Angew. Chem.* **2004**, *116*, 2890; *Angew. Chem. Int. Ed.* **2004**, *43*, 2830.

[11] a) H. O. Jeschke, M. E. Garcia, K. H. Bennemann, *Phys. Rev. A* **1996**, *54*, R4601; b) H. O. Jeschke, M. E. Garcia, K. H. Bennemann, *J Phys. B At Mol Opt Phys* **1996**, *29*, L545.

[12] W. D. Boo, Y. Ozaki, L. H. Andersen, W. C. Lineberger, *J. Phys. Chem. A* **1997**, *101*, 6688.

[13] I. Adrianov, V. Bonačić-Koutecký, M. Hartmann, J. Manz, J. Pittner, K. Sundermann, *Chem. Phys. Lett.* **2000**, *318*, 256.

[14] a) J. Manz, C. S. Parmenter, *Mode Selectivity in Unimolecular Reactions, Chem. Phys.* **1989**, *139* (special issue); b) J. Jortner, R. D. Levine, R. B. Pullman, *Mode Selective Chemistry*, Kluwer, Dordrecht, **1991**.

[15] a) C. N. Hinshelwood, *Proc. R. Soc. Lond. A* **1926**, *113*, 230; b) C. N. Hinshelwood, C. J. M. Fletcher, *Nature* **1933**, *24*, 131.

[16] A. Amirav, C. Horowitz, J. Jortner, *J. Chem. Phys.* **1988**, *88*, 3092.

[17] P. M. Felker, A. H. Zewail, *J. Chem. Phys.* **1985**, *83*, 2975.

[18] T. Leisner, S. Vajda, S. Wolf, L. Wöste, R. S. Berry, *J. Chem. Phys.* **1999**, *111*, 1017.

[19] H. Hess, S. Kwiet, L. Socaciu, S. Wolf, T. Leisner, L. Wöste, *Appl. Phys. B* **2000**, *71*, 337.

[20] R. Keller, F. Nöhmeier, P. Spädtke, M. H. Schönenberg, *Vacuum* **1984**, *34*, 31.

[21] C.-P. Huang, M. T. Asaki, S. Backus, M. M. Murnane, H. C. Kapteyn, *Opt. Lett.* **1992**, *17*, 1289.

[22] a) M. Hartmann, J. Pittner, H. van Dam, V. Bonačić-Koutecký, *Eur. Phys. J. D* **1999**, *9*, 393; b) M. Hartmann, J. Pittner, V. Bonačić-Koutecký, *J. Chem. Phys.* **2001**, *114*, 2106; c) S. Vajda, C. Lupulescu, A. Merli, F. Budzyn, L. Wöste, M. Hartmann, J. Pittner, V. Bonačić-Koutecký, *Phys. Rev. Lett.* **2002**, *89*, 213404.

[23] M. Hartmann, R. Mitrić, B. Stanca, V. Bonačić-Koutecký, *Eur. Phys. J. D* **2001**, *16*, 151.

[24] M. Hartmann, J. Pittner, V. Bonačić-Koutecký, *J. Chem. Phys.* **2001**, *114*, 2132.

[25] R. Mitrić, M. Hartmann, B. Stanca, V. Bonačić-Koutecký, P. Fantucci, *J. Phys. Chem. A* **2001**, *105*, 8892.

[26] a) D. Reichardt, V. Bonačić-Koutecký, P. Fantucci, J. Jellinek, *Chem. Phys. Lett.* **1997**, *279*, 129; b) V. Bonačić-Koutecký, M. Hartmann, D. Reichardt, P. Fantucci in *Recent Advances in Density Functional Methods, Part III* (Eds.: V. Barone, A. Bencini, P. Fantucci), World Scientific, Singapore, **2000**.

[27] R. Mitrić, M. Hartmann, B. Stanca, V. Bonačić-Koutecký, P. Fantucci, *J. Phys. Chem. A* **2001**, *105*, 8892.

[28] Y. Negeshi, Y. Nakamura, A. Nakajima, K. Kaya, *J. Chem. Phys.* **2001**, *115*, 3657.

[29] J. Hagen, PhD thesis, Freie Universität Berlin (Berlin), **2004**.

Received: September 21, 2004

